




# Iridium-Decorated Carbon Nanotubes as Cathode Catalysts for Li-CO<sub>2</sub> Batteries with a Highly Efficient Direct Li<sub>2</sub>CO<sub>3</sub> Formation/Decomposition Capability

Jun Wang<sup>1†</sup>, Yanjie Zhai<sup>2‡</sup>, Feng Dang<sup>1\*</sup>, Lanling Zhao<sup>3</sup>, Qing Xia<sup>1</sup>, Deyuan Li<sup>1</sup>, Dongdong Zhuang<sup>4</sup>, and Xiao Zhang<sup>2\*</sup>

<sup>1</sup> Key Laboratory for Liquid-Solid Structural Evolution and Processing of Materials (Ministry of Education), Shandong University, 17923 Jingshi Road, Jinan 250061, China

<sup>2</sup> Department of Mechanical Engineering, The Hong Kong Polytechnic University, Hung Hom, Kowloon, Hong Kong, China

<sup>3</sup> School of Physics, Shandong University, Jinan 250100, China

<sup>4</sup> School of Material Science and Engineering, Jiangsu University, Zhenjiang 212013, China

\* Corresponding author, E-mail: dangfeng@sdu.edu.cn; xiao1.zhang@polyu.edu.hk

## Abstract

Rechargeable Li-CO<sub>2</sub> batteries are regarded as the ideal application for the superior energy storage technology. However, they still limited by the lack of high efficiency electrocatalyst and limited understanding for the electrochemical reaction mechanism. In this work, we prepared the Ir-CNT composite by a rotation hydrothermal method, which remarkably promoted the reaction kinetics and enhanced the electrocatalytic performance of Li-CO<sub>2</sub> batteries. The incorporation of Ir nanoparticles shows high activity enhancement for the adsorption of Li<sub>2</sub>CO<sub>3</sub> species, which was confirmed by density functional theory (DFT) calculations. The Ir-CNT cathode exhibited an excellent ability to catalyze the formation and decomposition of Li<sub>2</sub>CO<sub>3</sub> during cycling. Therefore, a large specific capacity of 10325.9 mAh g<sup>-1</sup> and an excellent high rate cyclability with stably over 100 cycles were achieved. The three-dimensional Ir-CNT cathode could spontaneously advance the electrocatalytic activity of CO<sub>2</sub> oxidation and precipitation to increase specific capacities and cycle life, significantly boosting the practical application of Li-CO<sub>2</sub> batteries.

**Key words:** Li-CO<sub>2</sub> Batteries; Electrocatalysis; Cathode Catalyst; Ir-CNT Composite; DFT Calculations

**Citation:** Jun Wang, Yanjie Zhai, Feng Dang, Lanling Zhao, Qing Xia, et al. Iridium-Decorated Carbon Nanotubes as Cathode Catalysts for Li-CO<sub>2</sub> Batteries with a Highly Efficient Direct Li<sub>2</sub>CO<sub>3</sub> Formation/Decomposition Capability. *Materials Lab* 2022, 1, 220010. DOI: [10.54227/mlab.20220010](https://doi.org/10.54227/mlab.20220010)

## 1 Introduction

In response to traditional fossil fuel shortage and environmental pollution problem, the substitution of traditional energy consumption and carbon neutrality has become an international consensus. The development of new green power systems, such as supercapacitors and batteries, to satisfy increasing energy storage requirements is urgently needed. Among those, rechargeable Li-O<sub>2</sub> batteries (LOBs) have attracted more and more research attention because of their high theoretical energy density of 3500 Wh kg<sup>-1</sup>[1-3], and they are thus considered as a promising system to power the electric vehicles[4]. Generally, LOBs operate in the high-purity O<sub>2</sub> atmosphere, and previously reported results pointed out that they were extremely hard to work in an ambient air atmosphere with the influence of moisture and CO<sub>2</sub>[5,6]. It is demonstrated that CO<sub>2</sub> could react with discharge product Li<sub>2</sub>O<sub>2</sub> in the cathode, which eventually leads to the formation of by-product Li<sub>2</sub>CO<sub>3</sub> and worsens the electrochemistry performance of LOBs[7-9].

As early research conducted in 2011, Takechi *et al.* repor-

ted a Li/CO<sub>2</sub>-O<sub>2</sub> (from 0 to 100% volume CO<sub>2</sub>) battery[10]. Inspired by these results, Li-CO<sub>2</sub> batteries (LCBs) have been rapidly developed in recent years and show great potential for emerging high energy and power density applications[11,12]. Capturing and utilizing CO<sub>2</sub> as reactant gas based on the reversible reaction of 3CO<sub>2</sub> + 4Li<sup>+</sup> + 4e<sup>-</sup> ⇌ 2Li<sub>2</sub>CO<sub>3</sub> + C[13], LCBs could play an important role in reducing fossil fuel energy consumption and minimizing global climate changes caused by greenhouse effect. Moreover, CO<sub>2</sub> is much more soluble than O<sub>2</sub> in aprotic electrolytes, which is useful for promoting CO<sub>2</sub> reduction reactions, using CO<sub>2</sub> as a renewable energy carrier for CO<sub>2</sub> fixation and achieving a superior electrochemical performance[14,15]. In addition, LCBs have received intense attentions as the ideal energy source getting intense attentions for scientific exploration and future immigration to Mars, where the atmosphere contains 96% of CO<sub>2</sub>[16]. Actually, Li<sub>2</sub>CO<sub>3</sub> formed during discharge processes, however, is hard to be decomposed in the charge processes[17], leading to the large overpotentials of CO<sub>2</sub> evolution reaction and poor cycling stability[18,19]. Consequently, some strategies such as constructing efficient cathode catalysts[20,21] and improving bat-

Received 24 February 2022; Accepted 4 May 2022; Published online

‡ These authors contributed equally.

© 2022 The Author(s). *Materials Lab* published by Lab Academic Press

tery structures<sup>[22,23]</sup> are vitally significant to handle such challenges and boost the LCB performance<sup>[24]</sup>.

Tremendous efforts have been paid to explore a wide range of various catalysts, such as carbon-based materials<sup>[25,26]</sup>, metals<sup>[27,28]</sup>, metal oxides<sup>[29,30]</sup> and metal boride<sup>[31]</sup> with high electrocatalytic activity for LCBs. Among them, N-doping carbon supported noble metals<sup>[32,33]</sup> have been considered as promising candidate catalysts for LCBs. Zhou *et al.* utilized porous three-dimensional carbon nanotubes (CNTs) as the cathode catalysts, which delivered a discharge specific capacity of 6000 mAh g<sup>-1</sup> at 100 mA g<sup>-1</sup> and run for 22 cycles at 100 mA g<sup>-1</sup> with the fixed capacity of 1000 mAh g<sup>-1</sup><sup>[34]</sup>. Zhou *et al.* reported that graphene as the cathode catalyst showed a cycle life of about 10 cycles at 100 mA g<sup>-1</sup> with the fixed capacity of 1000 mAh g<sup>-1</sup> and the specific capacity of 6600 mAh g<sup>-1</sup><sup>[35]</sup>. However, the high charge overpotentials and poor cycling performance still existed in LCBs. In this regard, the design of Mo<sub>2</sub>C/CNTs with low overpotentials<sup>[36]</sup>, Ru@Super P with good cycling stability<sup>[18]</sup> and NiO/CNTs with remarkable oxidation efficiency<sup>[37]</sup> were conducted, demonstrating favorable electrocatalytic improvements of LCBs during the charge/discharge processes. Despite all this, achieving higher battery performance still remains challenging.

At present, Ir-based materials have been extensively studied as the cathode for LCBs. Ir is one of the most stable metals and a hyperactive oxygen evolution reaction catalyst in LOBs<sup>[38,39]</sup>. Firstly, A cathode based on reduced graphene oxide (rGO) with added Ir nanoparticles delivered a superior electrochemical activity toward the crystalline LiO<sub>2</sub><sup>[40]</sup>. It was also reported that Ir incorporated into deoxygenated hierarchical graphene exhibited excellent cycling performance in LOBs<sup>[39]</sup>. It is thus concluded that Ir-based material could contribute to decomposing Li<sub>2</sub>CO<sub>3</sub> during charging. Zhang *et al.* realized the complete decomposition of Li<sub>2</sub>CO<sub>3</sub> in LOBs using the Ir-decorated boron carbide (Ir/B<sub>4</sub>C) nanocomposite as a cathode material for LOBs, which displayed remarkably improved cycling stability<sup>[41]</sup>.

Herein, Ir-CNT composite was prepared by a rotating-hydrothermal method, and its catalytic activity for the bifunctional electrocatalytic properties in non-aqueous LCBs has been intensively investigated. For this composite, CNTs formed robust three-dimensional architecture, which provide a large specific surface area and storage space for discharge products. Then, the nano-sized Ir particles were homogeneously decorated on the network structure with abundant active sites. Ir-CNT cathode showed superior ability for catalyzing the formation and decomposition of Li<sub>2</sub>CO<sub>3</sub>, which could be attributed to the synergetic effects of the conductive three-dimensional CNTs and Ir nanoparticles with high electrocatalytic activities in the composite. CNT network could not only effectively enhance the electrical conductivity of the composite, but also offer enough regions for the tri-phase (solid-liquid-gas) reactions and accommodated huge volume changes during cycling. The well-dispersed Ir nanoparticles on the CNTs matrix could make full use of their high catalytic activity and promote more efficient CO<sub>2</sub>/Li<sub>2</sub>CO<sub>3</sub> conversion on the surfaces of the composite, giving a novel direction toward the cathode design and CO<sub>2</sub> electrocatalysis optimizing for LCBs.

## 2 Materials and methods

### 2.1 Material Preparations

Typically, 30 mg of CNTs were dissolved in 25 mL distilled water under vigorous magnetic stirring to form a homogeneous mixture at 25 °C, followed by adding 0.1 g of PVP and 57.59 mg of IrCl<sub>3</sub>·3H<sub>2</sub>O with vigorous stirring for 1 h. Afterwards, the as-prepared suspension was transferred into a Teflon-lined stainless-steel autoclave and maintained at 180 °C for 12 h in a thermo-mighty stirrer. Finally, the resulting product was centrifuged with ethanol.

### 2.2 Characterizations

The morphology of the materials was investigated through a field-emission scanning microscope (FESEM, SU-70) equipped with an energy dispersive X-ray spectrometer (EDS) and a transmission electron microscope (TEM, JEM-2100F). The composition of the materials is tested by an X-ray diffractometer (Rigaku D/Max-r B) and FT-IR spectroscopy (Bruker Inc. Vector 22). A Bruker spectrometer (RFS 100/S) was used to test Raman spectra. A Vacuum Generator Scientific spectrometer (ESCA 2000) was used to collect The XPS (X-ray photoelectron spectroscopy) data. Thermogravimetric analysis (TGA) was proceeded in air condition using a Thermo-gravimetric analyzer (TGA/SDTA851e).

### 2.3 Electrochemical Measurements

90 wt% catalyst materials and 10 wt% poly (tetrafluoroethylene) were uniformly mixed in isopropanol. They were subsequently dropped onto a Toray carbon paper (TGP-H-060), and the cathodes were vacuum dried at 120 °C for 10 h. Electrocatalytic properties were investigated by CR 2032 coin-type cells, which were assembled inside a glovebox under an Ar condition (H<sub>2</sub>O<0.1 ppm, O<sub>2</sub><0.1 ppm) using the catalyst-based cathode and the Li anode, separated by the glassy fiber soaking with 1 M LiTFSI-TEGDME electrolyte. The cycling voltammetry (CV) measurements were tested through an electrochemical workstation (RST5002F) with the condition at 0.1 mV s<sup>-1</sup> between 2.0-4.5 V. Galvanostatic discharge-charge tests were launched on a LAND battery tester (LANHE CT2001A). All battery measurements were tested at 25 °C and in a high-purity CO<sub>2</sub> condition.

### 2.4 DFT Calculations

The thermodynamically abundant (111) surfaces of Ir that are dominant on the wulff crystal have been established. For comparison, CNT (002) surfaces were also tested in the simulations. All the simulations were performed on basis of Density Functional Theory (DFT) calculations with plane-wave technique implemented in the Vienna ab initio simulation package (VASP)<sup>[42]</sup>. Gradient corrected exchange-correlation functional of Perdew, Burke and Ernzerhof (PBE) models were engaged to conduct the spin-polarized calculations under the projector augmented wave (PAW) method, with a cut-off kinetic energy of 400 eV for plane wave basis. The convergence criterion of the total energy was set up to be within 1×10<sup>-5</sup> eV, while all the atoms and geometries were optimized.

Ir (111) and CNT (002) were optimized energetically most favorable structures after the full geometry relaxation were conducted within a K-point 5×5×5 grid. The adsorption energy of CO<sub>2</sub>/Li<sub>2</sub>C<sub>2</sub>O<sub>4</sub>/Li<sub>2</sub>CO<sub>3</sub> is defined as E<sub>abs</sub>=E<sub>T</sub>-E<sub>A</sub>-E<sub>S</sub>, where

$E_T$  is the total energy of the corresponding system with specified atoms or molecules adsorbed, and  $E_A$  and  $E_S$  are the energy of the specified atom or molecule and the pristine system, respectively.

### 3 Results

Ir-CNT composite was synthesized via a rotating-hydrothermal method, as demonstrated in Figure 1. Its morphology was characterized by FESEM and TEM. As shown in Figure S1 image, the synthesized Ir-CNT composite consisted of numerous nanowires with a diameter of 10-20 nm. The element mapping of green C and red Ir elements in the EDS spectra demonstrates the uniform distribution of C and Ir in Ir-CNT composite in Figure 2d-2f. While for the detailed characterization of TEM, Figure 2a confirmed that the diameter of CNTs is about 10-20 nm, and the Ir nanoparticles are evenly decorated on the CNT surfaces. Notably, the three-dimensional Ir-CNT composite could enable multiple spaces for sufficient mass transport and discharge product storage, which aids in stabilizing electrode structure for guaranteeing stable and fast diffusion of  $\text{Li}^+$  and  $\text{CO}_2$  during reversible formation/decomposition of discharge products, and these Ir nanoparticles could act as active sites to play a key electrocatalytic

role in boosting  $\text{Li-CO}_2$  reactions. The result of the high-resolution lattice fringes in Figure 2b displays an interlinear spacing of 0.22 nm, corresponding to the (111) crystal plane of Ir<sup>[43]</sup>. The radial profiles of the selected area electron diffraction (SAED) and crystalline structure of the nanoparticles corresponded to C (002), Ir (111), (200) and (311) planes in Figure 2c, which are matched well with the reference patterns of graphitic carbon and Ir (JCPDS#46-1044). These results together with the XRD data proved the successful formation of Ir nanoparticles on the composite sample via the reported preparation route.

The Ir-CNT composite and CNTs were characterized by XRD. It can be seen from Figure 3a that both the diffraction peak of CNTs and the Ir-CNT composite exhibited diffraction peaks at around  $26^\circ$ , corresponded to the C (002) crystal plane<sup>[44]</sup>, and another relatively obvious diffraction peak of the Ir-CNT composite corresponds to the crystal Ir (111) crystal plane (JCPDS No.46-1044)<sup>[45]</sup>, which also illustrates the successful decoration of Ir nanoparticles. To further analyze the state of the metal element in the Ir-CNT composite, we carried out further XPS characterization. Figure 3b exhibits the 4f spectrum of the Ir element<sup>[39]</sup>. Specifically, the high-resolution XPS spectrum of Ir 4f were dominated by Ir (0)  $4f_{5/2}$  and Ir (0)  $4f_{7/2}$ , respectively. Meanwhile, the presence of Ir (IV)  $4f_{5/2}$  and Ir (IV)

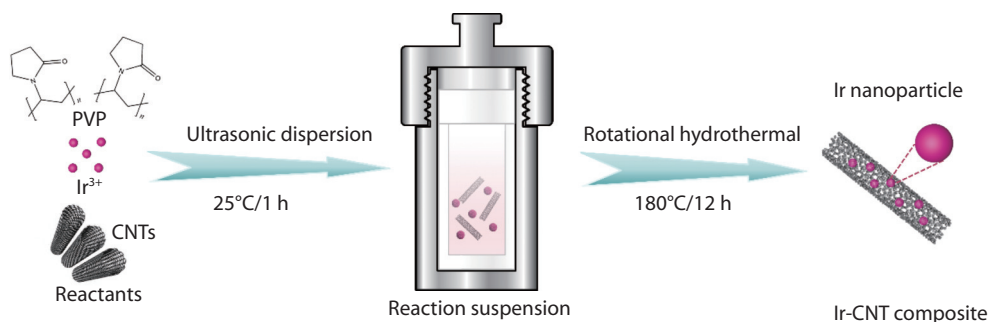


Fig. 1 Schematic representation of preparing Ir-CNT composite.

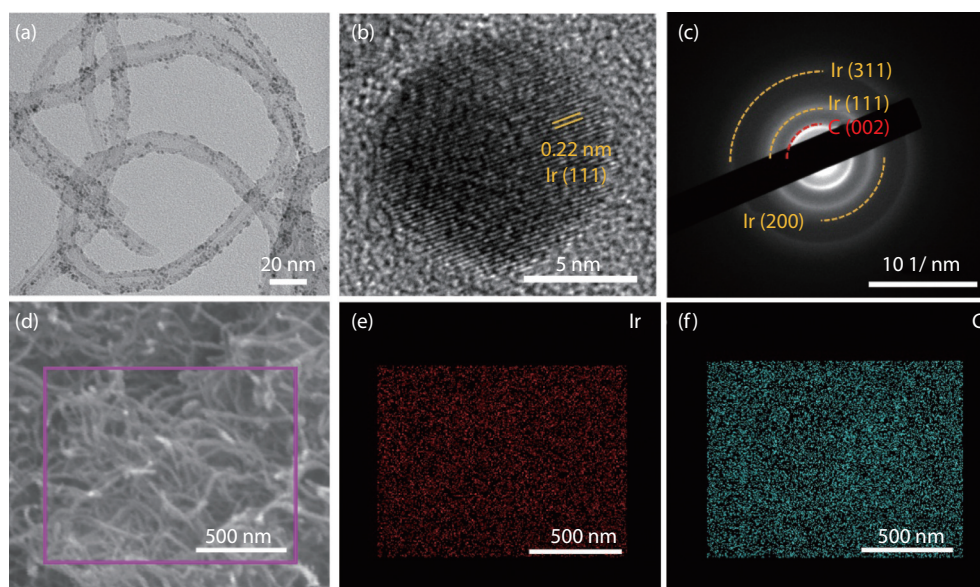
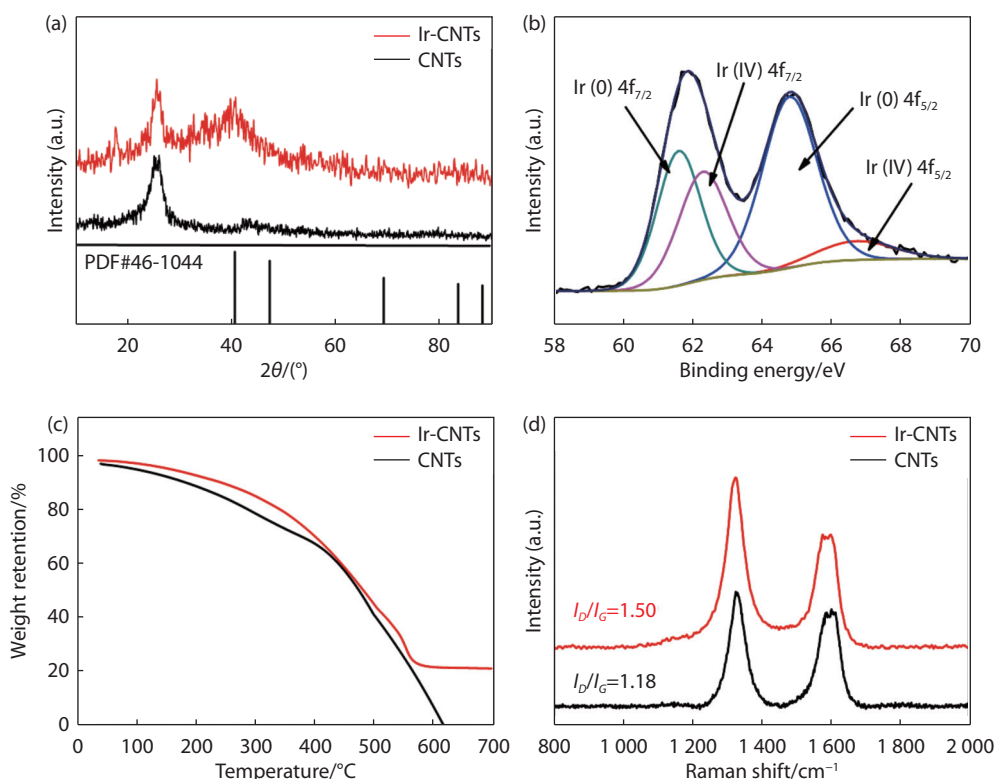


Fig. 2 (a,b) TEM images with (c) SAED pattern and (d) SEM image with EDS element mapping images of (e) Ir and (f) C elements of the Ir-CNT composite.

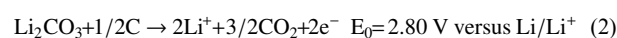
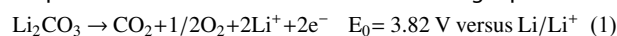


**Fig. 3** (a) XRD, high-resolution (b) Ir 4f XPS spectra, (c) TGA and (d) Raman data of Ir-CNT composite.

$4f_{7/2}$  signals indicate their surface oxidation, which is a common phenomenon in Ir nanoparticles. TGA measurement was performed from 20–700 °C at a temperature increase rate of 10 °C min<sup>-1</sup> under an air atmosphere to determine the content of IrO<sub>2</sub> nanoparticles in the composite. Based on this, the doping content of Ir nanoparticles can be calculated to be 19.36 % (Figure 3c). Raman D band peak and G band peak are connected with the structural defects in the graphitic structure and in-plane vibration of graphitic carbon, respectively. The  $I_D/I_G$  value was used to characterize the graphitic or disorder states aspects. Figure 3d showed the Raman spectrum<sup>[45,46]</sup> of the composite, and the  $I_D/I_G$  intensity ratios of Ir-CNTs and CNTs are 1.50 and 1.18, respectively, demonstrating that its graphitization degree increased due to the incorporation of Ir nanoparticles on CNTs.

The electrocatalytic activity of Ir-CNT cathode in LCBs was investigated, and the results are shown in Figure 4. As depicted in Figure 4a, the CNT cathode delivered a low discharge specific capacity of 8354 mAh g<sup>-1</sup>, while the discharge specific capacity of Ir-CNT cathode reached 10325.9 mAh g<sup>-1</sup>. It is found that CNT cathode exhibited limited specific capacity, mainly due to its limited active sites and poor electrocatalytic activities on the reduction activity of CO<sub>2</sub>. While for the Ir-CNT cathode, the charge and discharge specific capacity is almost the same, which reveals its superior property for the highly catalyzing decomposition of the discharge products for LCBs. The rate capability of Ir-CNT cathode was also tested with a cut-off voltage window of 2.0–4.5 V at different currents, as shown in Figure 4b. At the current densities of 100, 200 and 400 mA g<sup>-1</sup>, the discharge specific capacities are 10325.9, 5222.1 and 3851.4 mAh g<sup>-1</sup>, respectively. Figure 4d–4e showed the cycling stability of CNT and Ir-CNT cathodes at a

current density of 100 mA g<sup>-1</sup> with a cutoff specific capacity of 1000 mAh g<sup>-1</sup>. The CNT cathode displayed excessively higher charge overpotentials and fast discharge terminal voltage breakdown after 30 cycles, while the Ir-CNT cathode could be stably discharged and charged for almost 100 cycles (Figure 4f). Those demonstrated the as-prepared Ir-CNT cathodes with abundant active sites could realize the excellent charge and discharge stability. Then, the impedances raised to 220 Ω at the end of 1st discharging, owing to the generation of discharged products. After fully recharging, the resistance of the electrode declined as the reversible decomposition of discharged products. Particularly, only a slightly growing impedances of 120 Ω can be seen after 100 cycles, which is consistent with its outstanding cycle performance (Figure S2). In addition, we used CV to further investigate the electrocatalytic activity of CNT and Ir-CNT cathode for rechargeable LCBs. Compared with CNT cathode (Figure 4c), it is worth noting that the CV curve of Ir-CNT cathode showed an obvious CO<sub>2</sub> reduction peak<sup>[47]</sup>. In contrast, the profile of the Ir-CNT cathode exhibited a strong oxidation peak at around 4.1–4.3 V, mainly due to the advanced catalytic reactions, and there was no peak appeared in the CNT curve, because of the slow reaction kinetics of the insoluble Li<sub>2</sub>CO<sub>3</sub> decomposition. The CV results fully indicated that the Ir-CNT composite not only facilitated the reduction of CO<sub>2</sub>, but also played a vital role in the decomposition reaction of Li<sub>2</sub>CO<sub>3</sub>. The possible reactions are listed in the following equations<sup>[48]</sup>:



Eventually, the outstanding performance of the Ir-CNT cathode can be attributed to the synergistic effect of three-di-



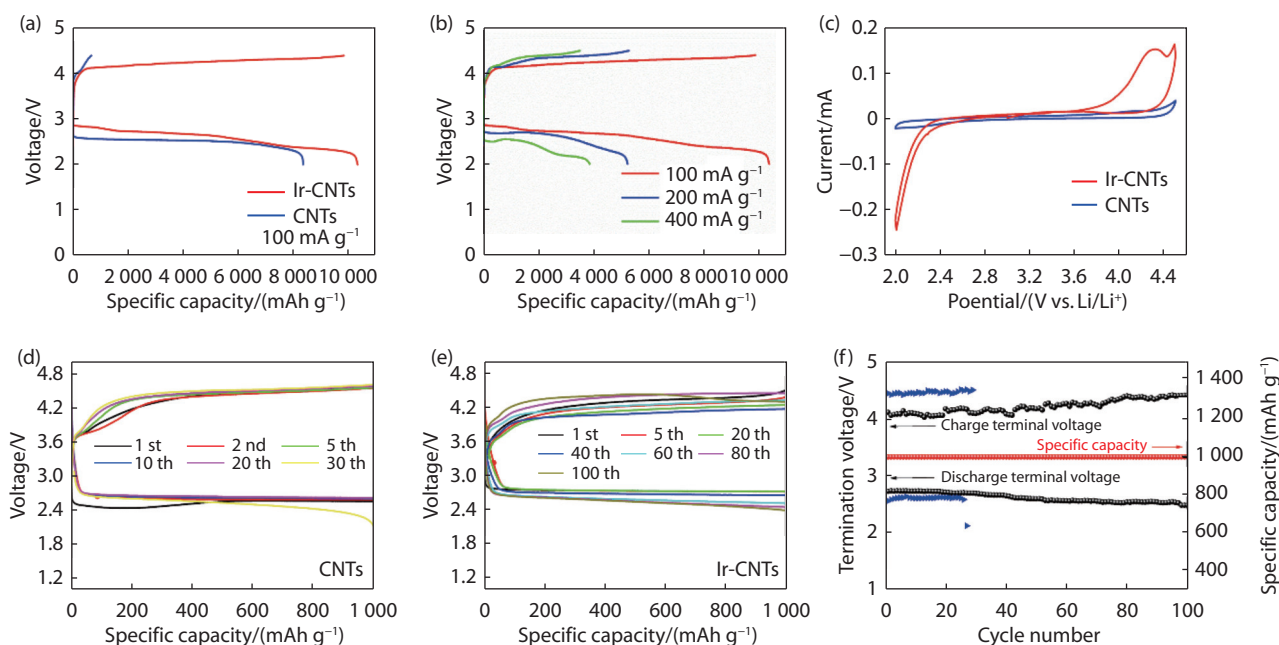


**Fig. 4** (a) Initial discharge/charge profiles at  $100 \text{ mA g}^{-1}$  and (c) CV curves of CNT and Ir-CNT cathodes; (b) rate capability of Ir-CNT cathodes at 100, 200 and  $400 \text{ mA g}^{-1}$ ; (f) cycling performance with typical discharge/charge profiles of (d) CNT and (e) Ir-CNT cathodes with a fixed capacity of  $1000 \text{ mAh g}^{-1}$  at  $100 \text{ mA g}^{-1}$ .

dimensional architecture and uniformly distributed Ir nanoparticles. The Ir-CNTs with optimized designed structure enhanced the discharged products formation and decomposition, which is the key point for a superior cycle performance than those of other works in Table 1.

To further investigate the states of the Ir-CNT cathodes for LCBs during cycling, *ex-situ* FESEM, TEM and XRD were characterized<sup>[49]</sup>. As shown in Figure 5a, after the discharge process, film-like products adhered to the surfaces of Ir-CNT cathode, and there is a diameter increase, compared with that of the pristine cathode material in Figure 2a. This conclusion can also be confirmed by *ex-situ* TEM image in Figure 5e that the diameter of the Ir-CNT composite and discharged product composite became 20–30 nm, meanwhile the layer thickness of discharged product reached about 10 nm. The diffraction rings of C (002), Ir (111),  $\text{Li}_2\text{CO}_3$  (002) and (311) crystal faces could be detected from SAED data<sup>[50]</sup> in Figure 5f. Furthermore, the crystalline nature of the discharge products on the Ir-CNT cathode surfaces were analyzed utilizing XRD measurement, and the results were illustrated in Figure 5d. The diffraction peaks of Ir-CNT cathode at the first complete discharging corresponded to (002), (-112), (020), (310) and (112) planes, which were assigned to the diffraction peak of the  $\text{Li}_2\text{CO}_3$  (JCPDS 83-1454). FTIR spectra of Ir-CNT cathode with the stage 1st discharging/charging were also studied in Figure S3. The results indicated the increased peak of the production of  $\text{Li}_2\text{CO}_3$  (C–O bond) after discharging and the disappearance of the peak after charging<sup>[51]</sup>. Therefore, it is concluded that the existence of discharged products and good reversible performance. After the first fully charging after 100 cycles, the diffraction peak of  $\text{Li}_2\text{CO}_3$  disappeared, indicating that the discharge products almost completely decomposed, benefiting from the excellent electrocatalytic performance of the Ir-CNT cathode. The same conclusion can be also drawn from the FESEM data. After the discharge process, the  $\text{Li}_2\text{CO}_3$

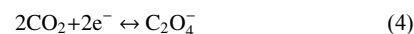
layer on the surface of Ir-CNT cathode seemed to disappear in Figure 5b, and the cathode almost maintained its original morphology after 100 cycles, as depicted in Figure 5c. This verified the pleasant cycling performance of the Ir-CNT cathode.

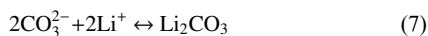
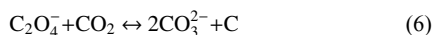
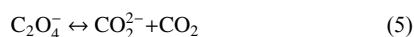
The electrocatalytic activity of Ir-CNT cathode was illustrated based on XRD, FESEM and TEM measurement results, and the possible mechanisms on the reversible formation and decomposition of discharge products were intensively discussed. It is widely reported that the operation of LCBs experiences the reversible formation by means of the follow reversible electrocatalytic reaction<sup>[52,53]</sup>:



Unfortunately,  $\text{Li}_2\text{CO}_3$  is a wide bandgap insulator, which is insoluble in nonaqueous LCBs. Therefore, its deposition on the cathode at discharging could result in an increase of impedance until "sudden death", which is similar to the deposition of  $\text{Li}_2\text{O}_2$  produced in nonaqueous LOBs during discharging. Normally in the charge process, it could lead to high overpotentials of  $\text{Li}_2\text{CO}_3$  decomposition, and develop novel catalyst materials is thus essential to reduce the high overpotentials to enhance battery efficiency. Similarly,  $\text{Li-O}_2$  and  $\text{Li-[O}_2+\text{CO}_2]$  batteries experience the formation of  $\text{Li}_2\text{O}_2$  and  $\text{Li}_2\text{CO}_3$  insulators and form active  $\text{O}_2^-$  and  $\text{O}_2^{2-}$  intermediates. Peeling oxygen from the  $\text{Li-[O}_2+\text{CO}_2]$  battery operation environment would induce LCB system<sup>[54]</sup>, which tends to exhibit excellent energy storage efficiency and the superior ability to capture and release  $\text{CO}_2$ .

Although the intermediate-involving processes is still unclear, it is assumed that disproportionation reactions of LCBs would also occur<sup>[55]</sup>, and the final products of these LCBs can be generated according to the (4)–(7) reactions:





DFT calculations were further carried out to verify the possibility of stable formation of  $\text{Li}_2\text{C}_2\text{O}_4$  intermediates on the surfaces of Ir nanoparticles<sup>[56]</sup>. Figure S4 provides the models

of  $\text{Li}_2\text{CO}_3$  monomer,  $\text{Li}_2\text{C}_2\text{O}_4$  monomer and Ir (111), respectively. The adsorption energy models were also established to obtain the binding energies of  $\text{Li}_2\text{CO}_3$  monomer to Ir (111) plane (Figure 5g) and  $\text{Li}_2\text{C}_2\text{O}_4$  monomer to Ir (111) plane (Figure 5h). It is evident that on the Ir (111) surfaces, the adsorption energy of  $\text{Li}_2\text{CO}_3$  reached 3.44 eV, while that of  $\text{Li}_2\text{C}_2\text{O}_4$  only achieved 1.81 eV.

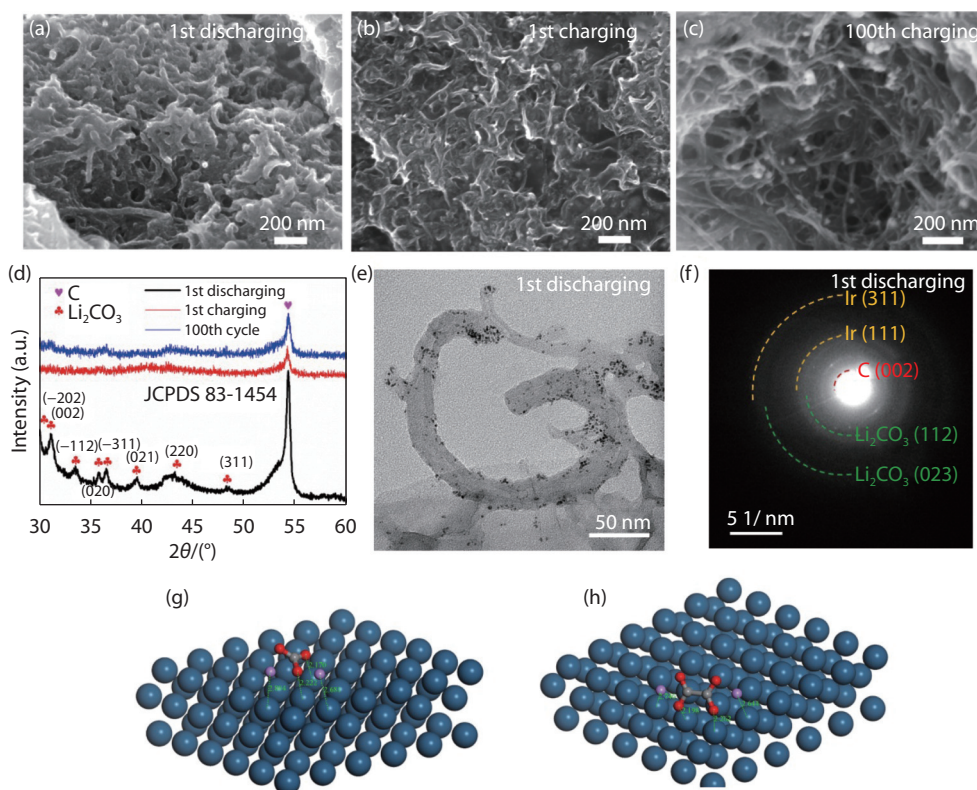


**Fig. 5** Ex-situ FESEM images of Ir-CNT cathodes at (a) 1st discharging, (b) 1st charging and (c) 100th charging stage; (e) ex-situ TEM image and corresponding (f) SAED pattern at 1st discharging; (d) XRD data of Ir-CNT cathodes at different stages; (g, h) comparison of adsorption energy between  $\text{Li}_2\text{C}_2\text{O}_4$  and  $\text{Li}_2\text{CO}_3$  monomer on Ir (111).

According to the calculation results of the adsorption energy, the Ir nanoparticles on Ir-CNT cathodes could serve as active centers, effectively capturing the final discharge product  $\text{Li}_2\text{CO}_3$  and promoting the electrocatalytic performance of LCBs. As  $E_{\text{ad}}/\text{Li}_2\text{CO}_3+\text{Ir}(111)$  is larger than  $E_{\text{ad}}/\text{Li}_2\text{C}_2\text{O}_4+\text{Ir}(111)$ , the surfaces of Ir-CNT cathode are more likely to enable  $\text{Li}_2\text{CO}_3$  accumulation, and the reversibility of discharge products was realized at charging and discharging in LCBs. Figure S5 showed the charge density difference of different adsorbates on the surface of Ir (111) to understand the electronic characteristics of the cathode surfaces and their interaction with different adsorbates. Yellow and blue contours represent the increased and decreased electron density, respectively. It can be concluded that Ir (111) could show strong interaction with the  $\text{Li}_2\text{CO}_3$ , forming a more stable bond with the substrate, which further verified the fact that Ir-CNT cathode could exhibit favorable  $\text{CO}_2$  electrocatalytic properties.

## 4 Conclusions

In general, Ir nanoparticles were dispersed onto the CNT

support by using a rotating hydrothermal method, which showed excellent catalytic activity in non-aqueous LCBs. In this composite, the CNTs formed a robust web-like structure, on which the nano-sized Ir particles were uniformly spread. The Ir-CNT cathode exhibited an excellent ability to catalyze the formation and decomposition of  $\text{Li}_2\text{CO}_3$  during cycling. We also analyzed the material structure, morphology and composition evolution on the Ir-CNT composite by XRD, Raman, XPS, FESEM and TEM measurements. A series of electrochemical performance tests were performed on Ir-CNT cathode for LCBs, including specific capacities, rate capability and cycling performance. It is evident that the incorporation of Ir nanoparticles showed remarkable activity enhancement for the adsorption of  $\text{Li}_2\text{CO}_3$  species, which was confirmed by DFT calculations. The three-dimensional Ir-CNT cathode could spontaneously and significantly promote the electrocatalytic activity of  $\text{CO}_2$  reduction and precipitation to improve specific capacities and cycling stability. Hence, it is concluded that the unceasing development of green and efficient electrocatalysts through various preparation strategies could play a vital role in further large-scale commercial applications of LCBs.

## Acknowledgments

Funding support is gratefully acknowledged from the China Postdoctoral Science Foundation (2020M672054), the Guangdong Basic and Applied Basic Research Foundation (2021A1515111124), the National Natural Science Foundation of China (52173286, U21A20311), the Natural Science Foundation of Shandong Province (ZR2020QB122) and the Young Scholars Program of Shandong University (2019WLJH21). Xiao Zhang acknowledges the start-up funding (BDC2) and Research Institute for Advanced Manufacturing (RIAM) Fund (CD4D) from the Hong Kong Polytechnic University.

## Conflict of interest

There are no conflicts to declare.

## Author contributions

Xiao Zhang, Feng Dang, Jun Wang and Yanjie Zhai conducted the research; Lanling Zhao, Qing Xia and Deyuan Li and Dongdong Zhuang analyzed the data; Jun Wang and Yanjie Zhai wrote the paper; all authors had approved the final version.

## REFERENCES

1. P. G. Bruce, S. A. Freunberger, L. J. Hardwick and J. M. Tarascon, *Nat. Mater.*, 2012, 11, 19
2. A. C. Luntz and B. D. McCloskey, *Chem. Rev.*, 2014, 114, 11721
3. N. N. Feng, P. He and H. S. Zhou, *Adv. Energy Mater.*, 2016, 6, 1502303
4. R. H. Zhang, Y. Li, M. Wang, D. W. Li, J. J. Zhou, L. Xie, T. Wang, W. Tian, Y. J. Zhai and H. Y. Gong, *Small*, 2021, 17, 2101301
5. J. J. Wang, Y. L. Li and X. L. Sun, *Nano Energy*, 2013, 2, 443
6. D. S. Geng, N. Ding, T. S. A. Hor, S. W. Chien, Z. L. Liu, D. Wu, X. L. Sun and Y. Zong, *Adv. Energy Mater.*, 2016, 6, 1502164
7. S. R. Gowda, A. Brunet, G. M. Wallraff and B. D. McCloskey, *J. Phys. Chem. Lett.*, 2013, 4, 276
8. Y. S. Mekonnen, K. B. Knudsen, J. S. Myrdal, R. Younesi, J. Højberg, J. Hjelm, P. Norby and T. Vegge, *J. Chem. Phys.*, 2014, 140, 121101
9. F. J. Li, T. Zhang and H. S. Zhou, *Energy & Environ. Sci.*, 2013, 6, 1125
10. K. Takechi, T. Shiga and T. Asaoka, *Chem. Commun.*, 2011, 47, 3463
11. X. F. Hu, Z. F. Li, Y. R. Zhao, J. C. Sun, Q. Zhao, J. B. Wang, Z. L. Tao and J. Chen, *Sci. Adv.*, 2017, 3, 7
12. Y. L. Liu, R. Wang, Y. C. Lyu, H. L. and L. Q. Chen, *Energy Environ. Sci.*, 2014, 7, 677
13. X. Li, S. X. Yang, N. N. Feng, P. He and H. S. Zhou, *Chin. J. Cat.*, 2016, 37, 1016
14. H. K. Lim, H. D. Lim, K. Y. Park, D. H. Seo, H. Gwon, J. Hong, W. A. Goddard, H. Kim and K. Kang, *J. Am. Chem. Soc.*, 2013, 135, 9733
15. Y. J. Zhai, J. Wang, Q. Gao, Y. Q. Fan, C. X. Hou, Y. Hou, H. Liu, Q. Shao, S. D. Wu, L. L. Zhao, T. Ding, F. Dang and Z. H. Guo, *J. Catal.*, 2019, 377, 534
16. Z. J. Xie, X. Zhang, Z. Zhang and Z. Zhou, *Adv. Mater.*, 2017, 29, 1605891
17. J. F. Sun, Q. Mu, H. Kimura, V. Murugadoss, M. X. He, W. Du, C. X. Hou, *Adv. Compos. Hybrid Mater.*, 2022
18. S. X. Yang, Y. Qiao, P. He, Y. J. Liu, Z. Cheng, J. J. Zhu and H. S. Zhou, *Energy Environ. Sci.*, 2017, 10, 972
19. J. M. Garcia-Lastra, J. S. G. Myrdal, R. Christensen, K. S. Thygesen and T. Vegge, *J. Phys. Chem. C*, 2013, 117, 5568
20. H. Yuan, S. W. Yang, Y. Hao, J. Y. Guo, W. C. Zhang, Q. Yu, X. Z. Yin, Y. Q. Tan, *Small Methods*, 2022, 6, 2200129
21. Z. S. Wang, H. Yuan, Y. Z. Zhang, D. D. Wang, J. P. Ju, Y. Q. Tan, *J. Mater. Sci. Technol.*, 2022, 101, 264
22. Y. B. Chen, Z. Li, D. D. Wang, H. Yuan, H. Z. Zhang, Y. Q. Tan, *Compos. Commun.*, 2021, 26, 100774
23. H. Yuan, G. Z. Li, E. H. Dai, G. L. Lu, X. Y. Huang, L. Y. Hao, Y. Q. Tan, *Chin. J. Chem.*, 2020, 38, 1767
24. Y. J. Zhai, H. Tong, J. L. Deng, G. Y. Li, Y. Hou, R. H. Zhang, J. Wang, Y. Y. Lu, K. Liang, P. Chen, F. Dang and B. Kong, *Energy Storage Mater.*, 2021, 43, 391
25. Y. L. Li, H. Yuan, Y. B. Chen, X. Y. Wei, K. Y. Sui, Y. Q. Tan, *J. Mater. Sci. Technol.*, 2021, 74, 189
26. Y. K. Zhao, Z. Yang, W. X. Fan, Y. C. Wang, G. Z. Li, H. L. Cong, H. Yuan, *Arab. J. Chem.*, 2020, 13, 3266
27. M. H. Li, Y. Y. Ma, J. Chen, R. Lawrence, W. Luo, M. Sacchi, W. Jiang, J. P. Yang, *Angew. Chem. Int. Ed.*, 2021, 133, 11588
28. E. H. Dai, G. Z. Li, G. X. Lu, W. Wang, Z. D. Han, Z. Y. Song, Q. Zhang, H. Yuan, X. Y. Zhang, *J. Ind. Text.*, 2020
29. Q. H. Deng, Y. Yang, S. Y. Qu, W. J. Wang, Y. K. Zhang, X. Y. Ma, W. W. Yan and Y. W. Zhang, *Energy Storage Mater.*, 2021, 42, 484
30. Y. P. Ma, X. B. Xie, W. Y. Yang, Z. P. Yu, X. Q. Sun, Y. P. Zhang, X. Y. Yang, H. Kimura, C. X. Hou, Z. H. Guo, W. Du, *Adv. Compos. Hybrid Mater.*, 2021, 4, 906
31. G. J. Zhu, R. Guo, W. Luo, H. K. Liu, W. Jiang, S. X. Dou, J. P. Yang, *Natl. Sci. Rev.*, 2021, 8, nwa152
32. Z. P. Han, X. Y. Zhang, H. Yuan, Z. D. Li, G. Z. Li, H. Y. Zhang, Y. Q. Tan, *J. Power Sources*, 2022, 521, 230956
33. G. Z. Li, H. Yuan, J. J. Mou, E. Dai, H. Y. Zhang, Z. D. Li, Y. K. Zhao, Y. F. Dai, X. Y. Zhang, *Compos. Commun.*, 2022, 29, 101043
34. X. Zhang, Q. Zhang, Z. Zhang, Y. N. Chen, Z. J. Xie, J. P. Wei and Z. Zhou, *Chem. Commun.*, 2015, 51, 14636
35. Z. Zhang, Q. Zhang, Y. N. Chen, J. Bao, X. L. Zhou, Z. J. Xie, J. P. Wei and Z. Zhou, *Angew. Chem. Int. Ed.*, 2015, 54, 6550
36. Y. Y. Hou, J. Z. Wang, L. L. Liu, Y. Q. Liu, S. L. Chou, D. Q. Shi, H. K. Liu, Y. P. Wu, W. M. Zhang and J. Chen, *Adv. Funct. Mater.*, 2017, 27, 1700564
37. M. S. Hong, H. C. Choi and H. R. Byon, *Chem. Mater.*, 2015, 27, 2234
38. S. Kumar, S. Chinnathambi and N. Munichandraiah, *New J. Chem.*, 2015, 39, 7066
39. W. Zhou, Y. Cheng, X. F. Yang, B. S. Wu, H. J. Nie, H. Z. Zhang and H. M. Zhang, *J. Mater. Chem. A*, 2015, 3, 14556
40. J. Lu, Y. Jung Lee, X. Y. Luo, K. Chun Lau, M. Asadi, H. H. Wang, S. Brombosz, J. G. Wen, D. Y. Zhai, Z. H. Chen, D. J. Miller, Y. Sub Jeong, J. B. Park, Z. G. Fang, B. Kumar, A. Salehi-Khojin, Y. K. Sun, L. A. Curtiss and K. Amine, *Nature*, 2016, 529, 377
41. S. Song, W. Xu, J. Zheng, L. Luo, M. H. Engelhard, M. E. Bowden, B. Liu, C. M. Wang and J. G. Zhang, *Nano Lett.*, 2017, 17, 1417
42. G. Kresse and J. Furthmüller, *Phys. Rev. B*, 1996, 54, 11169
43. H. S. Oh, H. N. Nong, T. Reier, M. Glied and P. Strasser, *Chem. Sci.*, 2015, 6, 3321
44. L. Geng, S. S. Xu, J. C. Liu, A. R. Guo and F. Hou, *Electroanalysis*, 2017, 29, 778
45. C. Y. Wang, Q. M. Zhang, X. Zhang, X. G. Wang, Z. J. Xie and Z. Zhou, *Small*, 2018, 14, 1800641
46. Y. J. Zhai, W. Y. Yang, X. B. Xie, X. Q. Sun, J. Wang, X. Y. Yang, N. Naik, H. Kimura, W. Du, Z. H. Guo and C. X. Hou, *Inorg. Chem. Front.*, 2022, 9, 1115
47. Y. Xing, Y. Yang, D. H. Li, M. C. Luo, N. Chen, Y. S. Ye, J. Qian, L. Li,

- D. J. Yang, F. Wu, R. J. Chen and S. J. Guo, *Adv. Mater.*, 2018, 30, 1803124
48. S. X. Yang, P. He and H. S. Zhou, *Energy Environ. Sci.*, 2016, 9, 1650
49. F. H. Ye, L. L. Gong, Y. D. Long, S. N. Talapaneni, L. P. Zhang, Y. Xiao, D. Liu, C. G. Hu and L. M. Dai, *Adv. Energy Mater.*, 2021, 11, 2101390
50. Y. J. Mao, C. Tang, Z. C. Tang, J. Xie, Z. Chen, J. Tu, G. S. Cao and X. B. Zhao, *Energy Storage Mater.*, 2019, 18, 405
51. M. H. Brooker and J. F. Wang, *Spectrochim Acta A Mol. Spectrosc.*, 1992, 48, 999
52. Y. Qiao, J. Yi, S. C. Wu, Y. Liu, S. X. Yang, P. He and H. S. Zhou, *Joule*, 2017, 1, 359
53. Z. Q. Zhuo, K. H. Dai, R. M. Qiao, R. Wang, J. P. Wu, Y. L. Liu, J. Y. Peng, L. Q. Chen, F. Pan, Z. X. Shen, G. Liu, H. Li, T. P. Devereaux and W. L. Yang, *Joule*, 2021, 5, 975
54. K. Nemeth and G. Srajer, *RSC Adv.*, 2014, 4, 1879
55. M. Goodarzi, F. Nazari and F. Illas, *J. Phys. Chem. C*, 2018, 122, 25776
56. J. W. Zhou, X. L. Li, C. Yang, Y. C. Li, K. K. Guo, J. J. Cheng, D. W. Yuan, C. H. Song, J. Lu and B. Wang, *Adv. Mater.*, 2019, 31, 1804439



©2022 The Authors. *Materials Lab* is published by Lab Academic Press. This is an open access article under the terms of the Creative Commons Attribution License, which permits use, distribution and reproduction in any medium, provided the original work is properly cited.